Energy & Environmental Science

PAPER

View Article Online
View Journal | View Issue

Cite this: *Energy Environ. Sci.*, 2016, **9**, 565

Development of solar fuels photoanodes through combinatorial integration of Ni–La–Co–Ce oxide catalysts on $BiVO_4$†

D. Guevarra,‡[a] A. Shinde,‡[a] S. K. Suram,[a] I. D. Sharp,[bc] F. M. Toma,*[bc] J. A. Haber*[a] and J. M. Gregoire*[a]

Received 17th November 2015,
Accepted 9th December 2015

DOI: 10.1039/c5ee03488d

www.rsc.org/ees

The development of an efficient photoanode remains the primary materials challenge in the establishment of a scalable technology for solar water splitting. The typical photoanode architecture consists of a semiconductor light absorber coated with a metal oxide that serves a combination of functions, including corrosion protection, electrocatalysis, light trapping, hole transport, and elimination of deleterious recombination sites. To date, such coatings have been mostly limited to simple materials such as TiO_2 and Co-Pi, with extensive experimental and theoretical effort required to provide an understanding of the physics and chemistry of the semiconductor-coating interface. To provide a more efficient exploration of metal oxide coatings for a given light absorber, we introduce a high throughput methodology wherein a uniform $BiVO_4$ thin film is coated with 858 unique metal oxides covering a range of metal oxide loadings and the full Ni–La–Co–Ce oxide quaternary composition space. Photoelectrochemical characterization of each photoanode reveals that approximately one third of the coatings lower the photoanode performance while select combinations of metal oxide composition and loading provide up to a 14-fold increase in the maximum photoelectrochemical power generation for oxygen evolution in pH 13 electrolyte. Particular Ce-rich coatings also exhibit an anti-reflection effect that further amplifies the performance, yielding a 20-fold enhancement in power conversion efficiency compared to bare $BiVO_4$. By use of *in situ* optical spectroscopy and comparisons between the metal oxide coatings and their extrinsic optical and electrocatalytic properties, we present a suite of data-driven discoveries, including composition regions which form optimal interfaces with $BiVO_4$ and photoanodes that are suitable for integration with a photocathode due to their excellent power conversion and solar transmission efficiencies. The high throughput experimentation and informatics provides a powerful platform for both identifying the pertinent interfaces for further study and discovering high performance photoanodes for incorporation into efficient water splitting devices.

Introduction

Conversion of solar energy to hydrogen *via* photoelectrochemical (PEC) water splitting offers a path toward storable and sustainable transportation fuels.[1] To harness sunlight and achieve spontaneous overall water splitting with reasonable efficiency, a dual junction configuration is needed to provide a net photovoltage of approximately 1.7–2 V to overcome kinetic limitations and other losses that compound upon the thermodynamically required 1.23 V.[1] For water splitting, much of this overpotential is needed for the oxygen evolution reaction (OER).[2,3] Since most semiconductor surfaces do not possess significant catalytic activity for the OER, it is necessary to incorporate a catalyst onto the surface of the semiconductor. The integration of a catalyst onto a semiconductor surface can improve PEC performance by enhancing catalytic activity and mitigating corrosion by physically separating semiconductors from the electrolyte and by efficiently extracting photogenerated carriers.[4] However, formation of a semiconductor/catalyst interface introduces additional complexity.[5] The energetics at the interface, presence of electronically active defects, electrical transport through the surface layer, light absorption or trapping properties, and chemical transformations in the operational environment can

[a] *Joint Center for Artificial Photosynthesis, California Institute of Technology, Pasadena, CA 91125, USA. E-mail: gregoire@caltech.edu, jahaber@caltech.edu*
[b] *Joint Center for Artificial Photosynthesis, Lawrence Berkeley National Laboratory, Berkeley, CA 94720, USA. E-mail: fmtoma@lbl.gov*
[c] *Chemical Sciences Division, Lawrence Berkeley National Laboratory, Berkeley, CA 94720, USA*

† Electronic supplementary information (ESI) available. See DOI: 10.1039/c5ee03488d

‡ These authors contributed equally to this work.

all influence PEC performance. Many of these characteristics of integrated photocatalytic assemblies emerge from specific materials interactions that cannot be readily predicted from the physical properties of the isolated components. For example, the distributions and populations of defect states at the interface depend on specific atomic scale interactions between the catalyst and semiconductor, which strongly depend upon composition, deposition method, and processing history.

Herein, we introduce a high throughput methodology and associated performance metrics for evaluation of catalyst/semiconductor assemblies as photoelectrodes. We illustrate this methodology and the utility of the performance metrics by experimentally generating, characterizing, and analysing a library of photoanode assemblies that each contain a thin film bismuth vanadate ($BiVO_4$) light absorber coated with an oxygen evolution catalyst. Combinatorial variation of the catalyst composition and loading yields a wide range of photoanode properties, most notably a class of catalyst/semiconductor combinations that exhibit significantly better performance than predicted from their electrocatalytic and optical properties in isolation. This unexpectedly high photoanode performance is indicative of beneficial interfacial processes, and our analysis reveals multi-functional behaviour of the best metal oxide coatings. The experimental design builds upon recent advances in high throughput OER catalyst synthesis and characterization, as well as the recent discovery of promising new Ce-rich quaternary oxides for OER catalysis.[6–9]

Combinatorial and high throughput methods have been developed for discovery and optimization of both complete devices and subcomponents for photovoltaics, fuel cells, batteries, *etc.*[10–12] Researchers have previously used scanning electrochemical microscopy to interrogate small libraries of catalysts on light absorbers,[13] and a recent combinatorial methodology was developed to evaluate 13 binary metal oxides as protective coatings on $BiVO_4$ in a concentrated carbonate electrolyte.[14] These initial studies motivate the development of larger scale combinatorial experiments and improved photoelectrochemical characterization to identify multi-functional catalyst/semiconductor interfaces. The methodology of the present work introduces the capability to automatically screen 858 photoanodes with an unprecedented combination of reliable photoelectrochemical and optical measurements. With the addition of advanced data processing, the high throughput methodology yields performance metrics that evaluate photoanode efficiency and suitability for pairing with a photocathode.

The application of a catalyst to the semiconductor surface can serve a number of roles: (1) improved OER kinetics yields rapid extraction of holes from the semiconductor, reducing the recombination current. (2) The catalyst/semiconductor interface alters the semiconductor surface to passivate electronically active defect states, thereby mitigating parasitic recombination. (3) Modification to the semiconductor interface energetics results in increased band bending within the semiconductor, reducing the majority carrier concentration and recombination rate.[15,16] The convolution of these factors makes the specific role of a catalyst on the PEC performance of semiconductor/catalyst assemblies ambiguous,[17] and requires application of advanced *in situ* methods to disentangle these processes.[15,16,18] Furthermore, recent work indicates that multiple factors can contribute to current density–potential (J–E) characteristics in parallel[18] and that the precise structure of the system is important.[19] However, these phenomena have only been investigated in detail on select materials combinations, particularly Fe_2O_3/Co-Pi interfaces. Generally-applicable predictive models are not yet available; therefore, synthesis and measurement remains necessary, particularly for complex, multi-component catalyst coatings.

The complexity of predicting the functional characteristics of semiconductor/catalyst junctions is further highlighted by the recent discovery of adaptive junctions.[20] For the case of dense and ion impermeable catalyst layers, the illuminated J–E response is defined by the solid state semiconductor/catalyst Schottky junction. However, for the case of sufficiently porous or permeable catalyst layers, bias- and illumination-dependent chemical transformations of the catalyst can significantly modify the junction energetics. As shown by Boettcher *et al.*, when the energetic position of the semiconductor valence band is significantly more positive than the thermodynamic potential for the OER, the illuminated J–E characteristics are not strongly dependent on the intrinsic activity of the dark electrocatalyst.[21] In this case, the functional characteristics of the assembly are primarily governed by the semiconductor/electrolyte junction energetics.

An important and outstanding challenge in photoanode research is the identification of semiconductor and catalyst properties that govern the regimes in which functional characteristics are dominated by (1) fixed and adaptive barrier heights, (2) intrinsic activity of the catalyst, and (3) recombination currents. Consequently, reliable prediction of the PEC performance of semiconductor/catalyst assemblies is not presently possible. Our study of catalyst coatings on $BiVO_4$ provides an important advancement in mapping relationships among individual material properties to integrated material properties, enabling further development of predictive models.

$BiVO_4$ is an excellent light absorber for this combinatorial study, as it is a promising transition metal oxide photoanode possessing a bandgap of $\sim$2.5 eV and a valence band position that is significantly more positive than the thermodynamic potential for OER.[22,23] Although the material suffers from poor majority carrier charge transport properties,[22,24–26] improved PEC performance has been enabled *via* impurity doping,[24,27–35] incorporation of electron selective contacts,[25,36–40] and utilization of mesostructured architectures.[36,37,39–42] Indeed, overall water splitting with a solar to hydrogen conversion efficiency of almost 5% under near-neutral conditions has been demonstrated by coupling an advanced gradient-doped $BiVO_4$ photoanode with amorphous silicon photovoltaics in a tandem structure.[27]

The bare surface of $BiVO_4$ possesses poor catalytic activity for the OER and a high concentration of electronically active defect states leading to significant photocarrier recombination losses.[32] Furthermore, the material suffers from chemical and photochemical instability under aqueous conditions.[43,44] To address these shortcomings, considerable effort has been devoted

to the integration of oxygen evolution catalysts onto the surface of $BiVO_4$. Under near-neutral conditions, where the material is most stable, a variety of catalysts have been integrated onto the surface,[45] including cobalt phosphate (Co-Pi),[13,27,46–50] cobalt oxide (CoO_x),[13,47,51] iron oxyhydroxide (FeOOH),[26,52,53] nickel oxyhydroxide (NiOOH),[41] nickel borate (Ni-Bi),[54,55] ruthenium oxide (RuO_2),[47] manganese oxide (MnO_x),[47] iridium oxide (IrO_x),[13,47] and platinum (Pt).[13] For the cases of Co-Pi and FeOOH in particular, the incorporation of a catalyst improves photoelectrochemical performance for oxygen evolution. The origin of this improvement has been attributed to suppression of electron–hole recombination at the interface.[27,46,48] However, it is important to note that electrocatalytic activity is not always predictive of PEC performance of $BiVO_4$/catalyst assemblies. For example, Bard and co-workers showed that integration of IrO_x, a highly active OER catalyst, onto the surface of $BiVO_4$ resulted in poor overall PEC activity.[13,26] Furthermore, Choi and co-workers have shown that using a dual layer of FeOOH, which improves interface quality, and NiOOH, which increases catalytic activity and affects Helmholtz layer formation, can greatly enhance the performance of $BiVO_4$ photoelectrodes.[41] While multicomponent coatings can help provide the numerous functions of a catalyst coating, mixed-metal oxide catalysts have been substantially underexplored, in part due to the lack of predictive models to guide selection of the vast materials space.

The studies of $BiVO_4$/catalyst assemblies described above were all performed under neutral or near-neutral electrolyte conditions. However, current solar hydrogen device architectures benefit from operation under strongly acidic or basic conditions to minimize polarization losses and enable the inclusion of a membrane to produce pure O_2 and H_2 product streams,[56,57] which are desired for safety and compatibility with end use applications. A few studies have investigated catalyst integration with $BiVO_4$ at pH 13. For example, atomic layer deposition (ALD) of CoO_x OER catalyst was found to considerably enhance PEC performance and improve short term chemical stability relative to bare $BiVO_4$.[58] Subsequent work explored the use of bilayer coatings composed of interfacial ALD TiO_2 films and sputtered Ni catalyst layers.[44]

These studies indicate that the operational window for catalysts on $BiVO_4$ photoanodes can be extended to highly alkaline conditions. Given the limited range of catalyst coatings studied to date, investigating a range of catalyst compositions to identify beneficial $BiVO_4$/catalyst interactions offers a significant opportunity for improving PEC performance. In our combinatorial study of inkjet-printed metal oxides on thin film $BiVO_4$, we identify catalyst compositions which create $BiVO_4$-based photoanodes whose performance under alkaline conditions (pH 13) is much higher than anticipated given the optical and catalytic properties of the catalyst. This approach employs data mining of high throughput datasets to identify the presence of interface-specific phenomena, which traditionally could only be identified through relatively slow and intensive surface science experiments. While the metal oxide coatings may provide a variety of interface and charge transport functions, they are referred to as catalyst coatings in this manuscript, in reference to the traditional purpose of metal oxide integration onto light absorbers.

Using the combinatorial, data-driven materials science approach for rapid identification of high-performance interfaces, we reveal compositions that exhibit both improved performance and stability. Importantly, the coating compositions that exhibit the highest PEC activity on $BiVO_4$ differ from those that exhibit the highest dark electrocatalytic activity. These observations are indicative of the complexity of semiconductor/catalyst assemblies and highlight the utility of combinatorial methods for discovering high performance photoanode assemblies. Furthermore, this approach will serve to greatly enhance the efficiency of experimental workflows in which combinatorial experimentation and data mining yield a representative set of unique interfaces that merit detailed characterization.

Experimental

$BiVO_4$ and library synthesis

To enable combinatorial investigation of catalyst coatings, the $BiVO_4$ light absorber was prepared using a spin coating technique that yields a uniform thin film with high performance within the class of undoped $BiVO_4$ thin films.[49] Such material is most suitable for the present study and we anticipate that the findings presented here could be incorporated into the design of higher efficiency systems that utilize state-of-the-art approaches to light absorber doping, nanostructuring, and heterostructuring. The $BiVO_4$ thin film was prepared on the fluorine doped tin oxide (FTO)-coated side of a 10 cm × 10 cm glass plate (TEC-15 Sigma Aldrich) following a literature protocol.[49] The glass plate was thoroughly washed with isopropanol (Sigma Aldrich, ≥98%), detergent (Alconex) in deionized water, and pure deionized water, dried with a nitrogen gun, and treated for 10 min with an ozone cleaner (Jelight Model 42) prior to deposition of $BiVO_4$. In a typical deposition, 15 mL of a 0.2 M solution of bismuth(III) nitrate pentahydrate (Sigma Aldrich, ≥98%) in acetylacetone (Sigma Aldrich, ≥99%) and 100 mL of a 0.03 M solution of vanadium(IV)-oxy acetylacetonate in acetylacetone were prepared separately and sonicated for 10 min. Then, the two solutions were mixed together and sonicated for an additional 5 min. Approximately 1–1.2 mL (enough solution to homogeneously cover the whole surface) of the resulting solution was filtered with 0.45 μm nylon filters (Thermo Fisher Scientific), and dispensed onto the 10 cm × 10 cm FTO/glass slide. The substrate was then spun twice in a row at 1000 rpm for 6 s on a spin coater (Laurell Technologies) with an acceleration rate of 150 rpm s^{-1}. After this spin-coating cycle, the substrate was annealed for 10 min in air at 500 °C in a muffle furnace (Cole-Parmer). This procedure (*i.e.* spin-coating followed by short annealing) was repeated nine times. After the last spin-coating cycle, the substrate was annealed for 2 h at 500 °C to achieve a final thickness of ~50 nm. Thickness determination was performed by Rutherford Backscattering Spectrometry (RBS), where He^+ ions were accelerated to 3040 keV on a 5SDH pelletron tandem accelerator manufactured by National Electrostatics Corporation (NEC)

with a sample tilt of 30–60° and backscattered ion detection at 165° using a Si surface barrier detector. Data fitting was performed with SIMNRA software. The correct pure-phase monoclinic $BiVO_4$ was verified by X-ray Diffraction (XRD) analysis using a Rigaku SmartLab diffractometer configured with parallel beam optics (see Fig. S1, ESI†).

The uniform light absorber plate served as the substrate for depositing the array of metal oxide coatings to create a library of photoanodes. A duplicate array of metal oxides was deposited onto a FTO-coated glass plate (without $BiVO_4$) to create a library of electrocatalysts. The composition library of mixed-metal oxide catalysts containing Ni, La, Co, and Ce was synthesized on each plate as a discrete library with 10 atom% composition steps in each element. Each of the 286 compositions in this quaternary composition space was deposited at 3 different catalyst loadings (designated L1, L2, and L3). The array of 858 metal oxide samples was deposited by inkjet printing at a resolution of 2880 × 1440 dpi, as described previously.[6,9] Elemental precursor inks were prepared by mixing 5 mmoles of each metal precursor with 0.80 g Pluronic F127 (Aldrich), 1.0 mL glacial acetic acid (T.J. Baker, Inc.), 0.40 mL of concentrated HNO_3 (EMD), and 30 mL of 200 proof ethanol (Koptec). The metal precursors were $Ni(NO_3)_2{\cdot}6H_2O$ (1.59 g, ≥98.5%, Sigma Aldrich), $La(NO_3)_3{\cdot}6H_2O$ (2.14 g, 99.999%, Sigma Aldrich), $Co(NO_3)_2{\cdot}6H_2O$ (1.49 g, 99.999%, Sigma Aldrich), and $Ce(NO_3)_3{\cdot}6H_2O$ (2.22 g, >99.0%, Sigma Aldrich). After inkjet printing the composition-loading library, the inks were dried and the metal precursors converted to metal oxides by calcination in air at 40 °C for 20 h, then at 70 °C for 27 h, followed by a 5 h ramp and 5 h soak at 350 °C. Previous characterization efforts have revealed that mixed-metal oxides prepared using these techniques are typically X-ray amorphous and can exhibit nanostructure that enables excellent OER electrocatalysis.[59] Integration of the metal oxides onto $BiVO_4$ poses substantial challenges for nanocharacterization, which is not addressed in the present work. The oxygen stoichiometry for each sample is not known and thus we refer to samples using the intended cation composition.

Each catalyst sample was synthesized over a 1 mm × 1 mm electrode area containing 0.75 nmoles of metal for loading L1, 1.9 nmoles of metal for loading L2, and 3.8 nmoles of metal for loading L3. The 858 catalyst samples were deposited along with additional duplicate (unused) samples on a square grid with 2 mm pitch. For the $BiVO_4$-coated plate, the array of samples was contained within an 8.8 cm-diameter circle centred on the 10 cm × 10 cm square plate.

For each loading, the 286 catalyst compositions were randomly distributed over the grid of sample positions. Consequently, any spatial or temporal artefacts in the PEC measurements were not convoluted with the effect of composition to produce an erroneous systematic composition-performance trend. Fig. 1a shows a photograph of the library on $BiVO_4$, with the library regions containing the L1, L2, and L3 loadings noted. Each sample in this library was characterized as an integrated $BiVO_4$-catalyst photoanode for water splitting, and is hereafter referred to as "the photoanode library". Each sample in the duplicate composition-loading library of catalysts deposited onto FTO/glass was characterized as an OER electrocatalyst and is hereafter referred to as "the catalyst library".

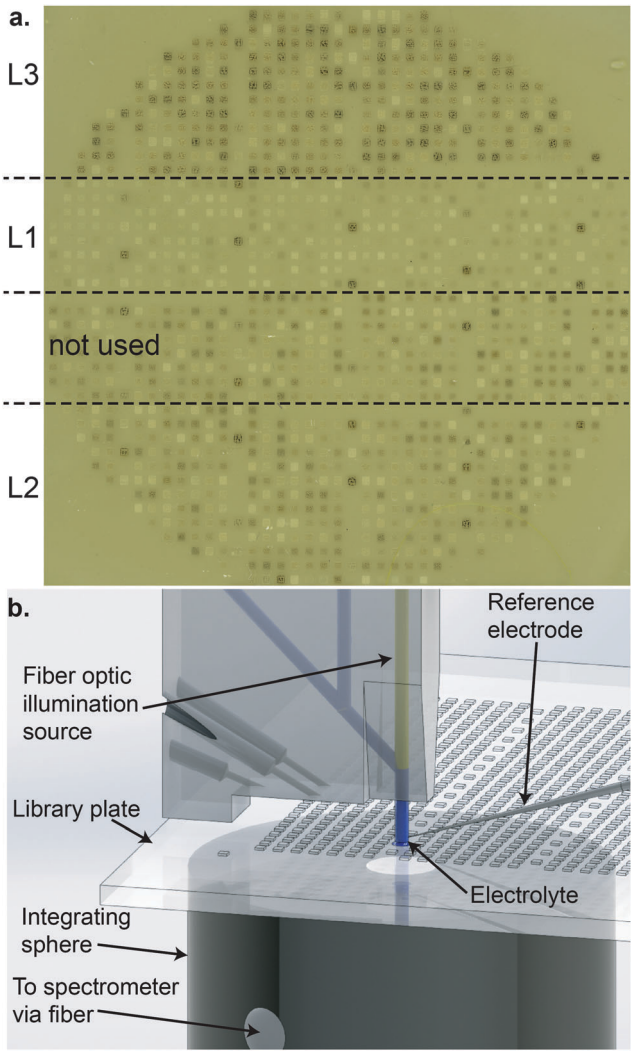

Fig. 1 (a) Photograph of the 10 cm × 10 cm FTO/glass plate with the $(Ni–La–Co–Ce)O_x$ catalyst library on $BiVO_4$. The regions of the library containing catalyst loadings L1, L2, and L3 are marked, with each of these regions containing the same 286 catalyst compositions. (b) Schematic of the scanning droplet cell (SDC) instrument in which the catalyst library is suspended between a 3-electrode electrochemical cell and an integrating sphere that collects transmitted light. The SDC contacts a single photoanode sample and is rastered across the library. Some SDC components have been removed for clarity.

Scanning electron microscopy (SEM) and energy-dispersive X-ray spectroscopy (EDS)

SEM characterization of the printed catalysts was performed with an FEI Nova NanoSEM 450. The compositions of binary samples in the $(Ni–La–Co–Ce)O_x$ quaternary library were measured with an EDS detector (Oxford Instruments X-Max 80) using a 15 keV electron beam and 6.5 mm working distance. SEM images were collected to investigate the microstructure of the as-prepared catalyst-coated $BiVO_4$, as shown in Fig. 2 for all six of the 1 : 1 binary compositions with the L3 loading.

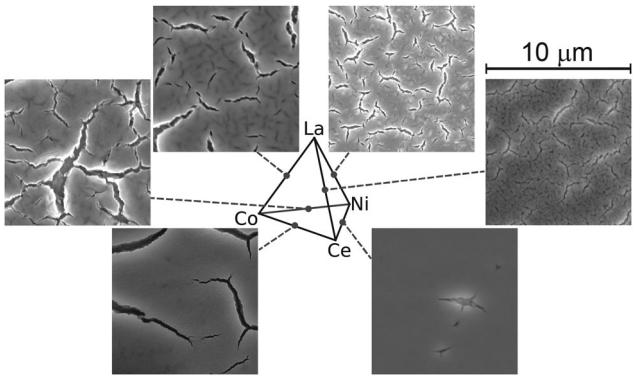

Fig. 2 The pseudo-quaternary catalyst composition space tetrahedron is shown with points marking the 1 : 1 mixtures along each of the 6 pseudo-binary lines. A scanning electron microscopy image (10 × 10 μm square) is shown for each of these compositions with the L3 loading, revealing the presence of 1 μm-scale cracks.

The catalyst compositions were confirmed to match the intended compositions by EDS of 15 samples selected from these 6 binary compositions at the 3 catalyst loadings (see Table S1, ESI†).

Additional characterization on the scaled-up electrode (described below) was performed with EDS measurements as described above and additional imaging was performed with a FEI QUANTA 250FEG SEM using a beam energy of 5 kV and an in-lens detector.

High throughput photoelectrochemistry

Scanning drop cell. The PEC and spectroscopic characteristics of the photoanode library were characterized using a custom-built scanning drop electrochemical cell (SDC) with integrated optical illumination and detection, as described previously.[60] The 3-electrode cell includes a Ag/AgCl reference electrode and Pt counter electrode controlled by a Gamry G 300 potentiostat and custom software. Electrochemical experiments were performed in aqueous 0.1 M sodium hydroxide with 0.5 M sodium sulfate as a supporting electrolyte (pH 13).

The SDC was suspended above the library plate and rastered over the array of library samples, as shown in Fig. 1b. A 0.4 mm-diameter optical fiber was integrated into the central port of the SDC and coupled to a xenon arc lamp (Newport 66921, 450 W), which included a liquid water filter to remove infra-red radiation (Oriel Instruments, 6123NS), neutral density filter (Rolyn Optics, #66.0220 50%T), and AM 1.5 filter (Newport, 81094). The bare fiber was placed in the electrolyte solution approximately 1 mm above the library plate, resulting in an illumination footprint of approximately 1 mm in diameter. The lamp calibration protocol is described in the ESI† and produced an absolute calibration of the illumination spectrum, with an estimated uncertainty of 15% (see Fig. S2, ESI†). The illumination irradiance is approximately 3.2 times that of AM 1.5 over the visible and ultraviolet wavelengths (390–900 nm). Over the spectral range absorbed by $BiVO_4$, (390–600 nm) the illumination is approximately 4 times greater than that of ASTM 6173-03 Global AM 1.5.

The PEC properties of the integrated photoanode library were characterized through toggled-illumination cyclic voltammetry (CV) measurements. In pH 13 electrolyte, the photoanode potential was swept from 1.23 to 0.585 V and back to 1.23 V *vs.* RHE (0 to −0.645 V and back to 0 V *vs.* O_2/H_2O) at a scan rate of 0.02 V s^{-1}. Illumination was toggled at 0.5 Hz (1.34 s on, 0.67 s off) so that a complete cycle of dark and illuminated current was completed at 0.04 V intervals. The data processing algorithm for the toggled-illumination CVs is described in detail in the ESI.† Briefly, each illumination cycle was interpreted by disregarding any sharp transients in the current during illumination toggling, and a cubic polynomial fitting routine was applied to the quasi-steady state currents to yield the illuminated and dark current signals for both the cathodic and anodic sweeps of the CV.

For many samples, significant transients in the illuminated current were observed during the first few illumination cycles of the cathodic sweep. This behaviour is similar to that of bare $BiVO_4$ electrodes and is likely due to the partial electrode area where $BiVO_4$ is exposed to the electrolyte. Due to this degradation after the initial cathodic sweep, all PEC properties of the photoanodes are obtained from the anodic sweep. Additional CV cycles performed on several samples confirmed that any further degradation in photocurrent proceeded slowly after the initial cathodic sweep. The dark current remained near zero for each analysed photoanode and in particular for the best performing photoanodes. Consequently, we assume that capacitive current was the main contribution to the dark current and calculate the photocurrent density ($J_{photo}(V)$) as the difference between the illuminated and dark current density signals.

The calculated $J_{photo}(V)$ signal was used to determine several performance metrics: J_{O_2/H_2O}, E_{OC}, and P_{max}. Evaluation of J_{photo} at 1.23 V *vs.* RHE (0 V *vs.* O_2/H_2O) produced J_{O_2/H_2O}, the photogenerated current density at the Nernstian potential for water oxidation. For many photoanodes, the photocurrent remained positive during the entire CV and thus an approximation of the open circuit photovoltage (E_{OC}) required extrapolation of the photocurrent signal, which is discussed further in the ESI.† The J_{photo} signal was also analysed to determine the maximum power point for each photoanode with respect to OER photoelectrocatalysis. This maximum power point refers to the particular values of E (E_{mp}) and J_{photo} (J_{mp}) corresponding to the maximum PEC power generation (P_{max}), under the assumption of 100% Faradaic yield for the OER.

The catalyst library on FTO-coated glass was characterized using the same SDC instrument to perform chronoamperometry (CA) measurements. Each catalyst sample was contacted using the same pH 13 electrolyte solution and held at an OER overpotential (η_{OER}) of 0.35 V for 25 s. For many catalyst compositions, a significant transient in the measured current was observed over the initial 5 s of the CA measurement, which we previously determined to be caused by oxidation of the metal oxides into their catalytically active states.[60] After this transient the current typically equilibrated, and the catalytic current density (J_{cat}) was evaluated to be the average current density over the final 1 s of the CA measurement. The samples

were illuminated during the CA measurements, and we confirmed that the photocurrent arising from the catalyst samples was negligible compared to the electrocatalytic current at this applied bias. The significant impact of adventitious incorporation of trace Fe contamination in the electrolyte on the activity of Ni-based OER catalysts has recently been well documented;[61–63] however, in the present study, perhaps due to the short duration of the electrochemical measurements, we did not observe any evidence of Fe incorporation.

In situ optical measurements

During each CA measurement (electrocatalyst library), and during the illumination periods of each CV measurement (photoanode library), the light transmitted through the sample was collected by an integrating sphere (Spectral Products AT-IS-1) approximately 1 mm below the bottom surface of the library plate, as depicted in Fig. 1b. The integrating sphere was fiber-coupled to a UV-vis spectrometer (Spectral Products SM303). The 8 mm opening of the integrating sphere collected all light transmitted by the photoanode or electrocatalyst samples with a scattering angle less than approximately 50°. All measurements were performed within an enclosure to block ambient light.

For the electrocatalyst library, the CA and optical transmission measurements were performed on bare regions of FTO-coated glass to define reference transmission spectra. For the photoanode library, the conformal $BiVO_4$ coating on the substrate precluded the acquisition of a reference spectrum on the library plate, so the reference transmission spectrum was acquired on a bare piece of the same type of FTO-coated glass plate. The dark signal from the spectrometer was also measured and used in conjunction with the reference transmission spectra to calculate the fractional transmission ($T(\lambda)$) for each transmission measurement (see ESI† for calculation details and examples of raw spectra and fractional transmission spectra).

For the CA measurements of the catalyst library, the transmission spectra were averaged over a 2 s interval at the end of the CA measurement to provide the fractional transmission spectrum (T_{cat}) of each catalyst after equilibration at 1.58 V *vs.* RHE (0.35 V *vs.* O_2/H_2O). For the CV measurements of the photoanode library, this optical characterization provided the fractional transmission spectrum (T_{anode}) of each $BiVO_4$-catalyst photoanode for each illumination cycle, using the final 0.67 s of the 1.34 s illumination period, thereby eliminating from these measurements the impact of any rapid transients in optical signals that occurred upon toggling the illumination. For approximately 3% of the photoanode library samples, the optical spectra were not available due to poor data quality. For analyses involving the *in situ* optical characterization of photoanodes, the corresponding figures exclude these samples.

Optical transmission efficiencies and consumed optical power

Here we define three optical parameters useful for evaluating the performance of catalysts and photoanode samples. The pertinent optical property of a given catalyst is its optical transmission, which determines the effective spectrum of light available for absorption by the underlying semiconductor. In particular, the catalyst coating should be highly transparent in the portion of the solar spectrum where the semiconductor is highly absorbing. The absorption spectrum of the bare $BiVO_4$ light absorber used in this investigation was characterized using a dual-integrating sphere instrument that measures the total spectral transmission and reflection.[64] The calculated fractional absorption spectrum ($A_{BVO}(\lambda)$) is shown in Fig. S2 (ESI†). This $BiVO_4$ photon absorption rate is a critical parameter for the photoelectrode since it defines the ideal light-limited current density. For a catalyst-coated $BiVO_4$ electrode, the expected number of photons absorbed by the $BiVO_4$ can be calculated from the product of the fractional transmission spectrum of a catalyst (T_{cat}), the fractional absorption of the $BiVO_4$ ($A_{BVO}(\lambda)$), and the photon flux of the incident light ($N_{Lamp}(\lambda)$). The corresponding optical transmission efficiency of the catalyst is given by the fractional transmission of photons that are expected to be absorbed by the $BiVO_4$:

$$\alpha_{T,cat} = \int_{\lambda_1}^{\lambda_2} T_{cat}(\lambda) A_{BVO}(\lambda) N_{Lamp}(\lambda) d\lambda \Big/ \int_{\lambda_1}^{\lambda_2} A_{BVO}(\lambda) N_{Lamp}(\lambda) d\lambda. \quad (1)$$

The wavelength integration range of 390 nm to 600 nm was chosen as the pertinent portion of the measurement spectrum with respect to the $BiVO_4$ band gap.

Since $BiVO_4$-based photoanodes are well suited for implementation in tandem light absorbers for anode-illuminated solar fuels generators,[27] it is important to consider the transmission of solar irradiation to an underlying photocathode. Consequently, we calculate the optical transmission efficiency for each photoanode (catalyst/semiconductor assembly) with respect to an unspecified photocathode light absorber that may use any transmitted solar irradiation in the 390–900 nm range. This calculation was performed by weighting the fractional spectral transmission (T_{anode}) by the ASTM 6173-03 standard for global air mass 1.5 spectral irradiance ($E_{AM1.5}(\lambda)$) and integrating over the wavelengths of interest (390–900 nm for our light source and spectrometer):

$$\alpha_{T,anode} = \int_{\lambda_1}^{\lambda_2} T_{anode}(\lambda) E_{AM1.5}(\lambda) d\lambda \Big/ \int_{\lambda_1}^{\lambda_2} E_{AM1.5}(\lambda) d\lambda. \quad (2)$$

It is worth noting the difference between $\alpha_{T,cat}$ and $\alpha_{T,anode}$. The former is a performance metric of a catalyst that quantifies the transmitted $BiVO_4$-absorbable photon flux under the experimental lamp irradiation, whereas $\alpha_{T,anode}$ is a performance metric of an integrated photoanode that quantifies the transmitted photocathode-absorbable irradiation under standard AM 1.5 illumination.

The transmission spectra of the photoanodes were also used to calculate the portion of the incident lamp irradiance that was not transmitted through the photoanode. In a tandem light absorber configuration, any photons reflected or absorbed by the photoanode are "consumed" by this portion of the device, and the total consumed optical power is given by

$$P_{consumed} = \int_{\lambda_1}^{\lambda_2} (1 - T_{anode}(\lambda)) E_{lamp}(\lambda) d\lambda, \quad (3)$$

where the $1 - T$ term is equivalent to the sum of the fractional absorption and reflection. This quantity is particular to the experimental lamp irradiation and defines an optical power against which a PEC power can be compared. That is, the ratio of P_{max} and $P_{consumed}$ is a type of power conversion efficiency, as discussed further below.

The optical spectra and scalar quantities are summarized in the glossary. To compare results from the photoanode library to that of bare $BiVO_4$, the high throughput protocol and data processing was applied to 3 regions of the library plate that were not coated with an inkjet-deposited catalyst. The average PEC and optical properties of these 3 samples represent the properties of the bare $BiVO_4$ film that underwent the same deposition and annealing history as each photoanode sample.

Scale-up and traditional photoelectrochemistry

The $La_{0.2}Co_{0.2}Ce_{0.6}O_x$ composition with the L2 loading was chosen for additional experiments using larger area electrodes. The $BiVO_4$ film preparation and inkjet printing conditions used for synthesizing the photoanode library were repeated to prepare a pair of about 1 cm^2 photoanodes. In order to expose FTO to provide electrical connection, an approximately 0.3 cm wide strip of the $BiVO_4$ thin film was etched away using 0.1 M HCl (Sigma Aldrich, ACS reagent, 37%). A Cu wire was connected to the exposed FTO using silver conductive epoxy (Circuit Works, CW2400), and the electrode with the attached wire was dried for 20 min at 60 °C. The wire was isolated with a glass tube, and the Cu wire, silver epoxy, and exposed FTO were all sealed together with the glass tube using a non-conductive, aqueous-resistant epoxy (Loctite 615 Hysol). Exposed surface areas of the assembled photoelectrodes were determined by optical scanning and digital image analysis with standard software (Image J). All PEC measurements were performed in a three electrode PEC cell with a planar quartz window (5 cm^2) using a BioLogic SP200 potentiostat. In the three-electrode PEC cell, the $BiVO_4$-catalyst photoanode, a coiled Pt wire, and a Ag/AgCl (3 M NaCl, BASI) were the working, counter, and reference electrodes, respectively. Measurements were performed in 0.1 M NaOH (Sigma Aldrich, ACS reagent, ≥97%) with and without the addition of 0.1 M of Na_2SO_3 (Sigma Aldrich, ACS reagent, ≥98%) as sacrificial reagent. All measurements under illumination were performed using simulated AM 1.5 light (Solar Light) adjusted to 100 mW cm^{-2} using a calibrated Si PV cell (SolarSim calibration, Newport).

Photoelectrochemical performance was established by running CV measurements from the open circuit potential to 1.7 V *vs.* RHE (0.47 V *vs.* O_2/H_2O) at a scan rate of 100 mV s^{-1}. Dark CV measurements were performed directly before the illuminated CV measurements and the measurement sequence was applied to both catalyst-coated and bare $BiVO_4$ electrodes. After the CV experiments, the photoelectrochemical stability of both of these electrodes was evaluated with a CA measurement at an applied bias of 1.23 V *vs.* RHE (0 V *vs.* O_2/H_2O) in the pH 13, 0.1 M NaOH electrolyte.

Results and discussion

Performance of integrated photoanodes

The PEC performance metrics of the photoanode library were evaluated using the anodic sweep of each high throughput toggled-illumination CV, an example of which is shown in Fig. 3a. The CV acquisition was performed at a throughput of approximately 35 s per photoanode, such that screening the entire library required less than 10 h. It is worth noting that the data quality rivals that of traditional photoelectrochemical measurement techniques and is amenable to automated calculation of the photocurrent. The photocurrent calculation and extraction of performance metrics are illustrated in Fig. 3b, and photocurrent signals from some of the best photoanodes are shown in Fig. 3c.

A common performance metric for photoelectrodes is the photocurrent density at the Nernstian potential of the applicable

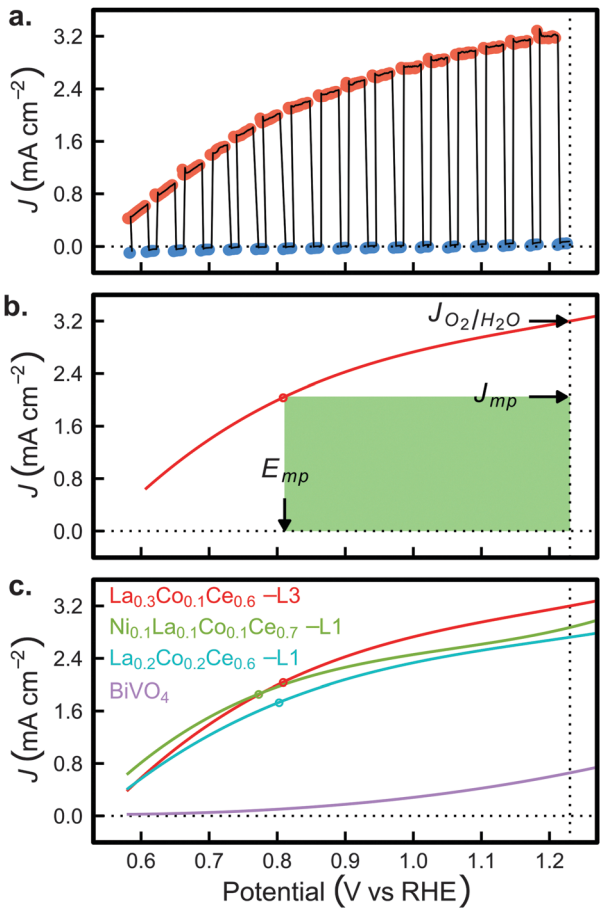

Fig. 3 (a) Anodic sweep of the CV acquired on L3 sample $La_{0.3}Co_{0.1}Ce_{0.6}O_x$ with illuminated (1.34 s) and dark (0.67 s) intervals highlighted in red and blue, respectively. (b) Disregarding the current transients upon illumination toggling, the photocurrent density is fit to a 3rd order polynomial (red line), providing the $J_{photo}(V)$ signal from which performance metrics are calculated. The short circuit current density (J_{O_2/H_2O}) is labelled as well as the maximum power point (red circle), which corresponds to an electrochemical power generation of P_{max} (shaded green area). (c) Representative photocurrent density signals from 3 of the best photoanodes are shown along with the photocurrent density signal from bare $BiVO_4$. The maximum power point is circled for each photoanode.

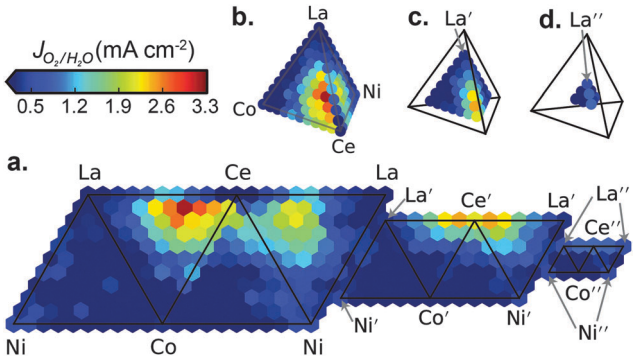

Fig. 4 Composition map of J_{O_2}/H_{2_O} for L3 samples. (a) The full pseudo-quaternary composition space is shown as the flattened set of pseudo-ternary faces with the 3 sets of 4 faces containing the compositions from the 3 concentric shells of the tetrahedron composition plot. These 3 shells of compositions are shown in (b)–(d), respectively, using the common false colour scale. The end-member compositions of the 3 shells are labelled M, M′ and M″ (where M = Ni, La, Co, or Ce), respectively. La′ corresponds to $Ce_{0.1}La_{0.7}Ni_{0.1}Co_{0.1}O_x$, La″ corresponds to $Ce_{0.2}La_{0.4}Ni_{0.2}Co_{0.2}O_x$. The definition of each composition label is provided in Table S1 (ESI†).

redox reaction, which is denoted as $J(E(A/A^-))$.[65] For characterizing photoanodes for the OER, the Nernstian potential of 1.23 V *vs.* RHE corresponds to the O_2/H_2O couple, and we denote the photocurrent at this potential as J_{O_2/H_2O}. The composition map of J_{O_2/H_2O} is shown for the L3 samples in Fig. 4. This figure uses a common false colour scale to show 2 different representations of the (Ni–La–Co–Ce)O_x composition space. Fig. 4a is the representation used throughout this article, where the entire pseudo-quaternary composition space is mapped using 3 connected sets of 4 pseudo-ternary triangles. The first set of 4 triangles comprises the 4 faces of the Ni–La–Co–Ce tetrahedron, as shown in Fig. 4b. Considering this set of compositions as the outer shell of the tetrahedron, the inner shells are shown in Fig. 4c and d, where each composition in these shells contains at least 10% and 20% of each element, respectively. The flattened composition map of Fig. 4a is obtained by unfolding these shells, and the vertices of the composition triangles are labelled by prime and double-prime element labels, which are defined in the figure caption and in Table S2 (ESI†). These 3 shells of composition points encompass the entire quaternary space with 10 atom% intervals.

The composition map of J_{O_2/H_2O} reveals that the (Ce–Co)O_x line contains the best pseudo-binary compositions. Local maxima are also found on the (Ce–Ni)O_x and (Ce–La)O_x lines, with each of these three binary composition spaces offering significant improvements over the constituent single metal oxides. The best pseudo-ternary compositions are obtained by adding Ni and, especially, Co to (La–Ce)O_x compositions. The local maxima in the (Ni–La–Ce)O_x and (La–Co–Ce)O_x composition spaces extend into the quaternary space around composition Ce′ ($Ni_{0.1}La_{0.1}Co_{0.1}Ce_{0.7}O_x$). These observations clearly demonstrate the promise of using mixed-metal oxide coatings to improve the photoanode performance of $BiVO_4$.

To further investigate the performance of the photoanodes, we turn our attention to the photocurrent obtained in reverse bias (below the O_2/H_2O potential). Under the assumption of 100% Faradaic efficiency for the OER, the electrochemical power generation is given by the product of this reverse bias potential and the corresponding photocurrent, which is readily calculated from the photocurrent data shown in Fig. 3. This quantity is often referred to as the power saved, although power saved is sometimes calculated using the potential difference between the photoanode and a dark electrocatalysts operating at the same photocurrent density.[65] In the present work we use the most conservative power-saved metric (yielding the smallest power-saved values) by referencing the photovoltage to the Nernstian potential of the OER.

The most meaningful scalar performance metric for a photoanode is its maximum electrochemical power generation (P_{max}), as illustrated in Fig. 3b. As noted above, the CVs in Fig. 3 do not extend to sufficiently cathodic potential to directly measure the open circuit potential. Since this is an important attribute of a photoanode, we discuss the calculation of E_{OC} in the ESI† and show the corresponding composition map in Fig. S6 (ESI†).

The map of P_{max} as a function of composition and catalyst loading is shown in Fig. 5. The trends in P_{max} are smooth with respect to composition and catalyst loading, demonstrating the fidelity of the high throughput measurements. The optimal loading is composition-dependent and similar composition trends are apparent among the 3 loadings. The composition region with highest P_{max} is centred on $La_{0.2}Co_{0.2}Ce_{0.6}O_x$. In this composition region, photoanodes in the 99th percentile of P_{max} (above 0.8 mW cm^{-2}) are found with all 3 loadings. The global maximum of 0.93 mW cm^{-2} is obtained with the $La_{0.2}Co_{0.2}Ce_{0.6}O_x$-L1 sample and is approximately 14 times larger than the 0.065 mW cm^{-2} provided by bare $BiVO_4$.

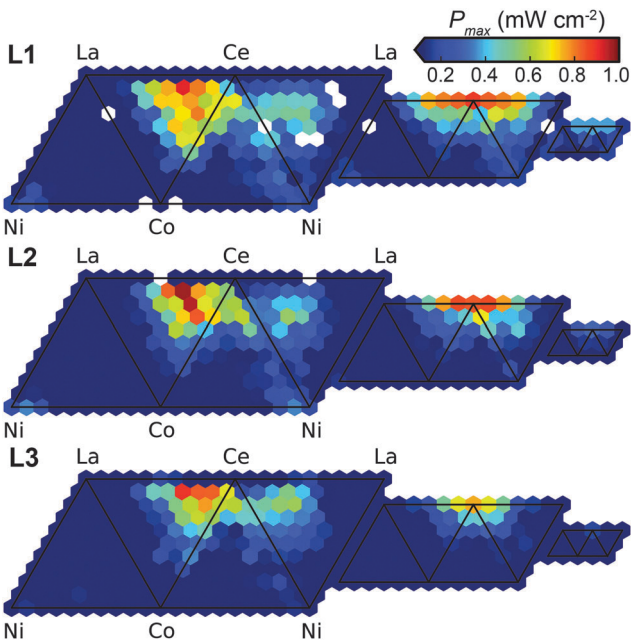

Fig. 5 Composition maps of P_{max} for all three catalyst loadings, plotted with a common colour scale using the flattened pseudo-ternary triangle scheme of Fig. 4a.

As previously reported[8] and discussed further below, the highest OER electrocatalytic activity in the $(La–Co–Ce)O_x$ composition space is obtained with more Co-rich, Ce-poor compositions.

Similarly, while the best pseudo-ternary OER electrocatalysts are found in the $(Ni–Co–Ce)O_x$ composition space,[6,8] no corresponding maximum in P_{max} is evident in Fig. 5. Instead, a local maximum in P_{max} is observed in the $(Ni–La–Ce)O_x$ pseudo-ternary face at $Ni_{0.3}La_{0.2}Ce_{0.5}O_x$. More Ni-rich compositions are not effective catalyst coatings on $BiVO_4$, and the highest P_{max} value with a Ni-containing catalyst coating is obtained with the higher-order composition $Ni_{0.1}La_{0.1}Co_{0.1}Ce_{0.7}O_x$ and L1 loading. This composition stands out among the quinary oxide samples in Fig. 5 and is discussed further below.

The P_{max} of bare $BiVO_4$ is in the 31st percentile of the photoanode library, meaning that approximately one third of the metal oxide coatings are deleterious to the PEC performance of $BiVO_4$. Applying mixed-metal oxide coatings does not generally lead to an improved photoanode and in fact less than 8.5% of the photoanode samples (70 of 828) exhibit P_{max} values in excess of 0.5 mW cm^{-2}, demonstrating that catalyst composition and loading must be carefully tailored to produce a high performance photoanode.

Validation using traditional techniques

To validate the results of combinatorial and high throughput experiments, a high performance photoanode catalyst composition and loading was selected from the combinatorial library and characterized using traditional techniques. The inkjet printing deposition technique offers the powerful ability to scale-up the electrode area using the same deposition conditions. Therefore, we resynthesized the $La_{0.2}Co_{0.2}Ce_{0.6}O_x$-L2, which was originally evaluated using high throughput methods on a 0.01 cm^2 sample, with a scaled-up area of approximately 1 cm^2. This electrode size is appropriate for incorporation into a traditional PEC cell coupled to a calibrated AM 1.5 light source.

CVs were acquired using the 1 cm^2 electrodes with and without illumination for catalyst-coated and bare $BiVO_4$ photoanodes in 0.1 M NaOH (pH 13) electrolyte, a standard technique for evaluating $BiVO_4$-based photoanodes in alkaline conditions.[44,58] The results are shown in Fig. 6a and confirm the substantial improvement in photoelectrocatalytic performance provided by the $La_{0.2}Co_{0.2}Ce_{0.6}O_x$ coating.

The integrated photoanode provides a photocurrent of 0.68 mA cm^{-2} and an open circuit photovoltage of approximately 0.81 V (0.42 V *vs.* RHE), rivalling the best values reported in pH 13,[58] and may be further improved upon optimization of deposition conditions. The shape of the CV under illumination is similar to the photocurrent density curves from the high throughput chopped-illumination CVs (Fig. 3c). The high throughput experiments were acquired with a $BiVO_4$-absorbable photon flux 4 ± 0.6 times larger than that of the AM 1.5 spectrum, which may result in the higher fill factor observed in the high throughput experiments. The photocurrent density at the OER potential is 2.4 mA cm^{-2} in the high throughput measurement, 3.5 times greater than in the traditional measurement, in agreement with the difference in illumination. This characterization of the scaled-up photoanode provides a robust validation of the high throughput result. To further investigate the PEC stability of the $La_{0.2}Co_{0.2}Ce_{0.6}O_x$-L2 photoanode, an illuminated CA experiment was performed at 1.23 V *vs.* RHE under AM 1.5 illumination for 2000 s. The stability results for the catalyst-coated and bare $BiVO_4$ photoanodes are shown in Fig. 6b. After 15 s, the photocurrent density of the $La_{0.2}Co_{0.2}Ce_{0.6}O_x$-L2 photoanode exceeds that of bare $BiVO_4$ by a factor of approximately 18, in agreement with the CVs acquired under illumination (Fig. 6a). Due to the rapid degradation of the bare $BiVO_4$, this improvement factor grows to a value of 70 at 500 s.

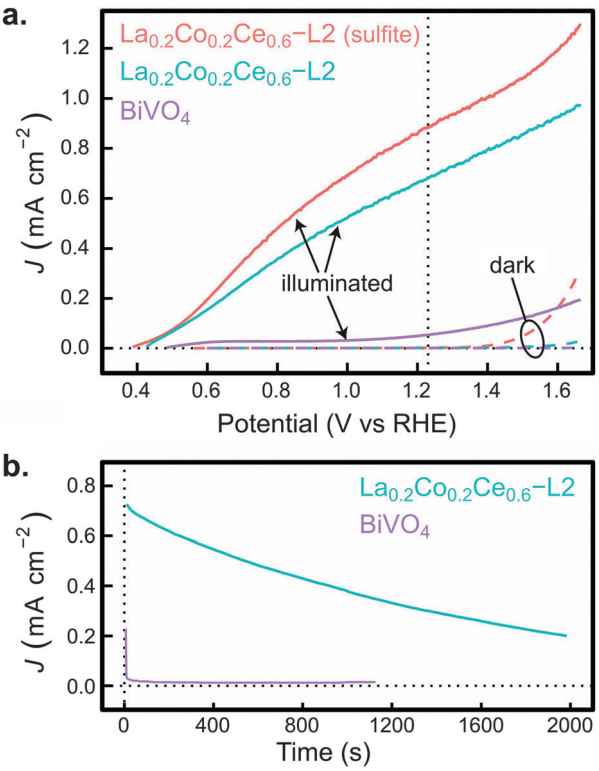

Fig. 6 (a) The anodic sweep from 6 CV measurements using a traditional cell and AM 1.5 light source. The illuminated (solid line) and dark (dashed line) current density are shown for bare $BiVO_4$ and for the scaled-up $La_{0.2}Co_{0.2}Ce_{0.6}O_x$-L2 sample; the latter sample was measured without and then with the addition of 0.1 M sulfite (Na_2SO_3) to the 0.1 M NaOH electrolyte. (b) The stability of the short circuit photocurrent density (1.23 V *vs.* RHE) of bare $BiVO_4$ and scaled-up $La_{0.2}Co_{0.2}Ce_{0.6}O_x$-L2 are measured under AM 1.5 illumination.

To characterize the coating morphology and any composition changes that occur from the extensive PEC experiments, SEM and EDS analysis of the scaled-up electrode was performed in both the as-prepared state (after calcination at 350 °C but prior to any electrochemical testing) and after PEC experiments. A $BiVO_4$ film without catalyst coating was also characterized, revealing a compact granular morphology of the light absorber. The catalyst coating is discontinuous and of variable thickness (see Fig. S16 and Table S3 in the ESI†). Within measurement error, the composition of the catalyst layer matches the intended composition of $La_{0.2}Co_{0.2}Ce_{0.6}O_x$ and is unchanged by the electrochemical

testing, demonstrating the fidelity of the combinatorial inkjet-based synthesis and the stability of this catalyst coating. While the composition of the $BiVO_4$ was unaffected by the catalyst deposition, the PEC testing increased the Bi : V ratio from 1 : 1 to 2 : 1. This significant loss of V is consistent with prior reports of the instability of $BiVO_4$ under basic conditions.[44]

While the $La_{0.2}Co_{0.2}Ce_{0.6}O_x$-L2 coating offers substantial improvement in the photoelectrocatalytic stability at pH 13, the degradation is still significant and appears to be caused by dissolution of V from the $BiVO_4$ light absorber. The inkjet printing method is optimized for the purpose of rapidly identifying promising candidate materials, not to produce conformal protective coatings. The significantly improved stability under alkaline conditions motivates future investigation of these catalyst compositions using alternate deposition techniques that provide conformal coverage of the $BiVO_4$, particularly because the EDS measurements suggest that the catalyst coating is itself quite stable.

Data-driven identification of optimal interfaces

A powerful use of the combinatorial screening of integrated photoanodes is to employ data-driven identification of catalyst compositions that exhibit unique interactions with the light absorber. Such catalyst/light absorber combinations are of particular interest for future scale-up and interface characterization to elucidate the interfacial properties that give rise to the excellent performance. To enable this data-driven study, the (Ni–La–Co–Ce)O_x composition and thickness library was synthesized on an FTO-coated glass substrate to characterize the optical and electrocatalytic properties of each catalyst (separate from the $BiVO_4$ light absorber). Using the catalytic activity and optical transparency of the catalysts under operation, a simple model was derived to predict the performance of the catalysts when integrated with $BiVO_4$.

Since the operational surface potential of the photoanode is unknown, we choose a representative OER overpotential of η = 0.35 V to map the OER catalytic current density (J_{cat}) over the catalyst library. Both directed and high throughput studies of OER metal oxide electrocatalysts in alkaline conditions have shown considerable darkening of the catalysts under operational conditions compared to ambient or as-synthesized conditions, which is understood to be due to oxidation of the catalyst.[60,66] Using *in situ* optical characterization under potentiostatic control, the optical transmission and catalytic activity of the catalysts were measured simultaneously after 25 s of polarization at 1.58 V *vs.* RHE (η_{OER} = 0.35 V). The optical transmission efficiency ($\alpha_{T,cat}$, eqn (4)) was then calculated as the fraction of the photons transmitted through the catalyst that are expected to be absorbed by the $BiVO_4$ thin film (390–600 nm), a methodology previously described in greater detail.[60]

For all 3 loadings of the (Ni–La–Co–Ce)O_x compositions, the values of J_{cat} are plotted relative to $\alpha_{T,cat}$ in Fig. 7 with the data points coloured according to P_{max} values of the equivalent metal oxide samples in the integrated photoanode library. The two primary properties of the metal oxides related to their function as coatings on a light absorber are optical

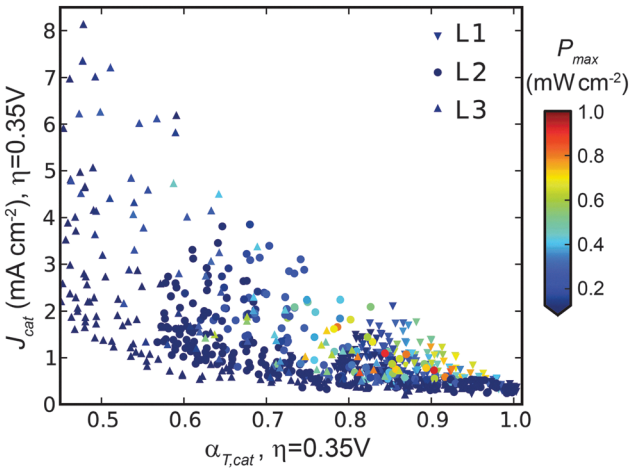

Fig. 7 Each of the 858 library samples is plotted according to the optical transmission efficiency ($\alpha_{T,cat}$) and catalytic activity (J_{cat}) measured on the FTO/glass-supported library. Each sample is coloured by the P_{max} measured on the $BiVO_4$ photoanode library. Each sample with high P_{max} (green to red colours) is surrounded by samples with much lower P_{max}, demonstrating the lack of a systematic relationship among $\alpha_{T,cat}$, J_{cat}, and P_{max}.

transparency and catalytic activity. Accordingly, one may expect that the performance of the integrated photoanodes (P_{max}) will vary systematically with $\alpha_{T,cat}$ and J_{cat}. However, Fig. 7 reveals that this is not the case, as low-P_{max} data points are intermixed with high-P_{max} data points. The lack of systematic variation of P_{max} for the integrated photoanode with respect to $\alpha_{T,cat}$ and J_{cat} of the dark electrocatalyst reveals that these parameters alone cannot be used to robustly predict the behaviour of integrated photoanodes. Indeed, composition-dependent interactions of the catalyst with the $BiVO_4$ light absorber strongly affect the photoanode performance. These high throughput results provide an important demonstration of the complex behaviour of material interfaces.

A variety of semiconductor photoelectrochemistry device models can be employed to predict photoanode performance from the individual properties of the light absorber and catalyst, but the non-systematic trends of Fig. 7 indicate that no such model will accurately predict the performance of the 858 photoanodes. However, by applying such a model we can make important observations about which catalysts outperform and underperform the model predictions. The level of over- or under-performance may indicate composition-dependant interfacial catalyst/light absorber interactions. We investigate these trends by mining our extensive electrochemical and optical datasets.

To predict the performance of an integrated metal oxide/$BiVO_4$ assembly, we apply a simple model that combines the optical transmission and catalytic performance of the metal oxide into a single predictive efficiency metric. As evident in Fig. 7, the range of catalytic current densities is much wider than the range of optical transmission efficiencies. Following the model used in previous work,[9,60] we estimate the intrinsically limited photocurrent that can be attained by the $BiVO_4$ thin film with the illumination source used in this work, which serves as a

maximum relevant current density (J_{max}) for calculating the catalytic efficiency of the electrocatalysts. That is, the parameter J_{max} represents the maximum useful catalytic current density because any catalytic current density greater than this value could not be produced by the integrated photoanode. For these catalysts integrated onto this $BiVO_4$ film we choose J_{max} = 3 mA cm^{-2}, which is among the highest values observed in Fig. 4. Inspection of Fig. 7 also shows that the electrocatalyst compositions with high P_{max} in the photoanode library exhibit catalytic current densities close to, but not exceeding, this value. The combined optical-catalytic efficiency ($\alpha_{C,cat}$) for integration onto $BiVO_4$ is calculated as the product of the optical transmission efficiency and catalytic current efficiency:

$$\alpha_{C,cat} = \alpha_{T,cat}(\mathrm{Min}[J_{cat}, J_{max}]/J_{max}). \quad (4)$$

This efficiency metric is in the range [0,1] and serves as a dimensionless predictor of photoanode performance based on properties of the catalysts measured separately from the $BiVO_4$. The composition maps of $\alpha_{T,cat}$, J_{cat}, and $\alpha_{C,cat}$ are shown in Fig. S8–S11 (ESI†) for all 3 catalyst loadings, and the results for the L3 samples are shown in Fig. 8a–c. Predicting absolute *J–E* characteristics of photoanodes would require more sophisticated models,[66] but eqn (4) captures the salient features of such models and serves the present purpose of quantifying the catalysts' relative predicted performance upon integration with the light absorber.

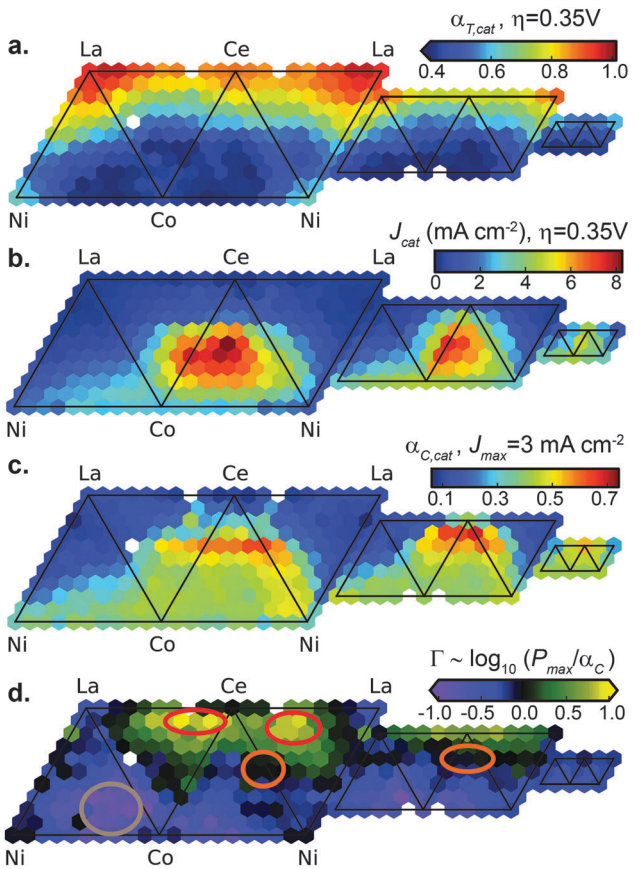

Fig. 8 Composition maps of (a) optical transmission efficiency ($\alpha_{T,cat}$), (b) catalytic current density (J_{cat}), and the ensuing (c) combined figure of merit ($\alpha_{C,cat}$) for the L3 catalyst samples from the FTO/glass-supported library. The parameter Γ compares photoanode performance (P_{max}) to that predicted by $\alpha_{C,cat}$, and the corresponding composition map is shown in (d).

To identify catalyst compositions that perform either well above or well below this expectation, the photoanode performance for each photoanode library sample can be compared to the combined optical-catalytic efficiency of the corresponding catalyst library sample, which we achieve through the quantities:

$$\Gamma' = \log_{10}(P_{max}/\alpha_{C,cat}), \quad \Gamma = \Gamma' - \mathrm{median}(\Gamma'). \quad (5)$$

The parameter Γ provides a log-scale quantification of the ratio of photoanode performance to the predicted catalyst efficiency, which for ease of interpretation is shifted to a median value of 0. A virtue of the use of the wide range of compositions and thicknesses in the combinatorial study is that we can use the median behaviour of the catalysts to calibrate the scale and subsequently analyse deviations from this median performance. The compositional maps of Γ are shown in Fig. S12 (ESI†) for all 3 catalyst loadings and in Fig. 8d for the L3 loading. With this analysis, values of Γ near 0 correspond to catalysts whose performance on $BiVO_4$ is comparable to what can be expected from the combined optical-catalytic efficiency. Fig. 8d contains 2 composition regions circled in orange which are the top-tier compositions from the $\alpha_{C,cat}$ values of Fig. 8c and whose high values of P_{max} in the integrated photoanode are commensurate with this prediction (Γ values near 0). The elemental oxides (Ni, La, Co, and Ce end members) also have Γ values near 0, indicating that none of these elemental oxides exhibit especially beneficial interactions with $BiVO_4$. Many compositions in the (Ni–La–Co)O_x space have substantial negative Γ values, with values approaching −1 in the composition region noted with a tan circle. These compositions have approximately one tenth the anticipated performance and suggest deleterious effects of the integration onto $BiVO_4$. The compositions with highest values of Γ (near 1) correspond to compositions which perform 10 times better than expected, and representative composition regions exhibiting this elite performance are circled in red. These compositions are related in that the sum of the Co and Ni composition is 10–20% and the balance is mixed La and Ce, with Ce being the largest component.

The composition trends of Γ are similar for all 3 catalyst loadings, largely due to the way in which the $\alpha_{C,cat}$ metric normalizes the loading-dependent trade-off between transparency and catalytic activity (see Fig. S8 and S9, ESI†). These results indicate that the composition regions marked in red in Fig. 8d form better interfaces with $BiVO_4$ than the other compositions and serve as excellent examples of interface discovery enabled by high throughput screening of the combined catalyst/light absorber library.

The role of Ce-rich metal oxide coatings

The data-driven quantification of interface quality indicates that (Ni–La–Co–Ce)O_x catalysts with 70–90 metal atom% Ce exceed their performance expectations, particularly since these metal oxides are neither the most transparent nor among the

best OER electrocatalysts. This result is supported by the traditional electrochemistry results of Fig. 6. To further investigate the photocatalytic performance of $La_{0.2}Co_{0.2}Ce_{0.6}O_x$-L2 on $BiVO_4$, the oxidation of 0.1 M sulfite (Na_2SO_3, a sacrificial hole-acceptor exhibiting facile oxidation kinetics) in pH 13 electrolyte was compared to water oxidation in pH 13 electrolyte. Under illumination, the difference in E_{OC} between the sulfite-containing and sulfite-free experiments is negligible, suggesting that photocarrier recombination rates at the $BiVO_4$/catalyst interface is comparable in the two cases and that the role of the metal oxide coating is primarily interfacial rather than catalytic. For $BiVO_4$, a light absorber with a fairly deep valence band, photogenerated holes are understood to be sufficiently energetic to perform the OER without an optimized electrocatalyst. However, $BiVO_4$ suffers substantially from high surface recombination rates, which can be alleviated through appropriate interface engineering. The high throughput chopped-illumination CVs (see Fig. 3a) provide additional evidence that the best catalyst/$BiVO_4$ assemblies exhibit reduced recombination rates compared to bare $BiVO_4$. The current transients upon illumination toggling, which are indicative of capacitive charging of surface states, are very low compared to bare $BiVO_4$ surfaces.

The lower photoanodic current in the sulfite-free electrolyte (Fig. 6) reveals that the $La_{0.2}Co_{0.2}Ce_{0.6}O_x$-L2/$BiVO_4$ photoanode suffers from limited reactivity for the OER, suggesting that incorporating an additional OER catalyst may further improve performance.[41] Importantly, the suite of high throughput and traditional photoelectrochemistry results demonstrate that the Ce-rich metal oxide coatings interface well with $BiVO_4$, motivating further investigation of the interface structure and its relationship to efficient charge separation and transport.

Predictions for tandem light absorber systems

An integrated $BiVO_4$-catalyst photoanode must be paired with a suitable photocathode to enable unassisted water splitting. Upon specification of the *J–E* characteristic of a photocathode and its spectral absorption, the high throughput spectral and photoelectrochemical data can be processed in a device model to identify the optimal photoanode. Implementation of specific device models is beyond the scope of this manuscript, but an important aspect of any device model with anode-facing illumination is the optical transmission of the photoanode assembly. To characterize the spectral properties of the photoanode library, we employ the *in situ* optical transmission data that was acquired during the high throughput CV measurements. A representative potential of 0.78 V *vs.* RHE (−0.45 V *vs.* O_2/H_2O) from the anodic sweep was chosen since this is a substantially cathodic potential where most of the photoanodes exhibit anodic photocurrent. From each transmission spectrum, the fraction of AM 1.5 irradiance transmitted by the photoanode ($\alpha_{T,anode}$) was calculated according to eqn (2), yielding the composition maps shown in Fig. 9. As with the composition map of $\alpha_{T,cat}$ at 1.58 V *vs.* RHE (+0.35 V *vs.* OER, Fig. 8a and Fig. S9, ESI†), the Co-rich compositions are the least transmissive and transparency generally increases with increasing concentration of the rare earth elements, La and Ce. One notable difference between

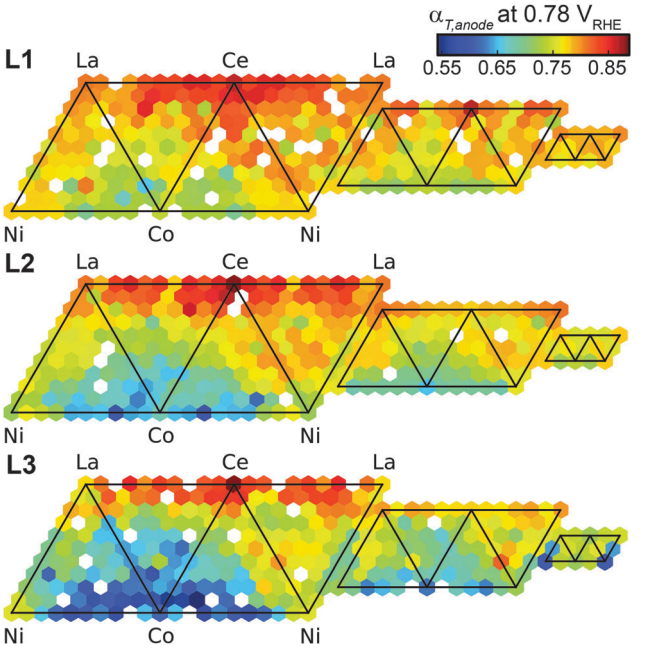

Fig. 9 Composition maps of the transmission efficiency ($\alpha_{T,anode}$) of AM 1.5 irradiance through each photoanode. The optical transmission spectrum for each sample was acquired *in situ* at 0.78 V *vs.* RHE during the anodic sweep of the chopped illumination CV.

these two transmission efficiencies is the relative increase in transparency of (Ni–Ce)O_x compositions in the photoanode library compared to the catalyst library, where the formation of Ni^{3+} may be supressed in the photoanode. The most striking feature in the $\alpha_{T,anode}$ data is the very high transparency of Ce-rich compositions. Whereas La-rich compositions exhibit the highest $\alpha_{T,cat}$, photoanodes, Ce-rich coatings exhibit the highest AM 1.5 transmission. The transmission efficiencies reach 0.89, which is significantly larger than the transmission efficiency of 0.79 exhibited by the bare $BiVO_4$ film under the same PEC conditions. This observation suggests that the Ce-rich oxide coatings may provide an anti-reflection of other light-trapping effect in addition to the beneficial interfacial interactions described in the previous section.

Power conversion efficiency

While a high value of $\alpha_{T,anode}$ is desirable with respect to transmission of solar irradiance to an underlying photocathode, the foremost requirement of a photoanode is the efficient utilization of the photons that are not transmitted. Any photons reflected or absorbed by the photoanode are consumed and no longer available to the photocathode portion of a tandem device. Measurement of the total consumed optical power is enabled by the *in situ* optical characterization reported here. The photoanode converts a fraction of the consumed optical power to chemical energy, and the value of this efficiency at the maximum power point is of particular interest:

$$\alpha_{P,anode} = P_{max}/P_{consumed}, \quad (6)$$

where P_{max} is the maximum electrochemical power generation (Fig. 5) and $P_{consumed}$ is calculated according to eqn (3) using the *in situ* measurement of spectral transmission from the CV illumination cycle closest to the maximum power point. While additional measurement of the spectral reflection would provide the capability to determine the photon absorption flux and thus the quantum conversion efficiency of the photoanode, the $\alpha_{P,anode}$ metric is desirable as it inherently includes the light management effects of the catalyst coating.

The composition map of $\alpha_{P,anode}$ is shown in Fig. 10 and demonstrates that several photoanodes produce power conversion efficiencies in excess of 3%. Compared to the P_{max} metric, the lowest loading performs better in the power conversion efficiency metric because the slightly lower P_{max} values are offset by a proportionally larger decrease in $P_{consumed}$. Only 7 photoanodes (less than 1% of the library samples) exhibit an efficiency in excess of 2.5%, and all of them have Ce concentrations in the range of 0.6–0.8.

The $La_{0.2}Co_{0.2}Ce_{0.6}O_x$-L2 library sample, which was chosen for the traditional PEC experiments, exhibits a P_{max} value of 0.93 mW cm^{-2} and a consumed optical power conversion efficiency of $\alpha_{P,anode}$ = 3.4%. This consumed optical power conversion efficiency is matched by a quinary oxide sample, $Ni_{0.1}La_{0.1}Co_{0.1}Ce_{0.7}O_x$-L1. While this quinary oxide sample exhibits a slightly lower P_{max} value of 0.85 mW cm^{-2} (approximately 13 times higher than that of bare $BiVO_4$), it is particularly interesting due to its high transmission (see Fig. S14, ESI†). The average transmission of the lamp irradiance is 79% for $BiVO_4$, which increases to 86% upon integration with $Ni_{0.1}La_{0.1}Co_{0.1}Ce_{0.7}O_x$-L1 (these values of lamp irradiance transmission are slightly different than the AM 1.5 transmission values of Fig. 9). This increased photoanode transparency translates to a decrease in $P_{consumed}$ by a factor of approximately 1.5 compared to bare $BiVO_4$, which corresponds to a substantial enhancement in the optical power available for use by a tandem photocathode. Several photoanode samples exhibit this high transparency, which is visually apparent in the photograph of the as-prepared library in Fig. 1a, where several samples appear whiter or lighter yellow compared to the bare $BiVO_4$ thin film. Among these samples, $Ni_{0.1}La_{0.1}Co_{0.1}Ce_{0.7}O_x$-L1 exhibits particularly good PEC performance (see Fig. 3c). The combination of decreased optical power consumption and increased PEC power generation compound to an improvement in consumed optical power conversion efficiency of a factor of 20 compared to the $\alpha_{P,anode}$ value of 0.17% for bare $BiVO_4$. These results demonstrate that the application of an optimal mixed metal oxide coating increases the photoanode efficiency through multiple mechanisms. The optical properties and power efficiency of this sample are discussed further in the ESI† (see Fig. S14 and S15, ESI†). Further investigation is required to ascertain whether the catalyst coating reacts with the $BiVO_4$ to alter its optical properties or the increased transparency is due solely to a light-trapping effect.

The largest improvements to photoanode efficiency are only attained for catalyst coatings containing 3 or 4 metal elements, demonstrating the significant opportunity, as well as the considerable challenge, associated with exploring the role each element plays in creating an optimal interface to $BiVO_4$. Achieving a more fundamental understanding of catalyst/semiconductor assemblies, particularly those utilizing mixed-metal oxide catalysts, will require contributions from both experimental and theoretical interface scientists. From known properties of these metal oxides, it is difficult to conjecture whether each element performs a unique function or if their combination conspires to simultaneously passivate deleterious $BiVO_4$ surface states, enable efficient hole transport from the $BiVO_4$ to OER reaction sites, introduce high OER catalytic activity, and manage light efficiently. The high throughput experimentation and informatics approach presented here provides a powerful platform for identifying the pertinent interfaces that should be studied in greater detail to enable rapid leaps in both understanding and performance.

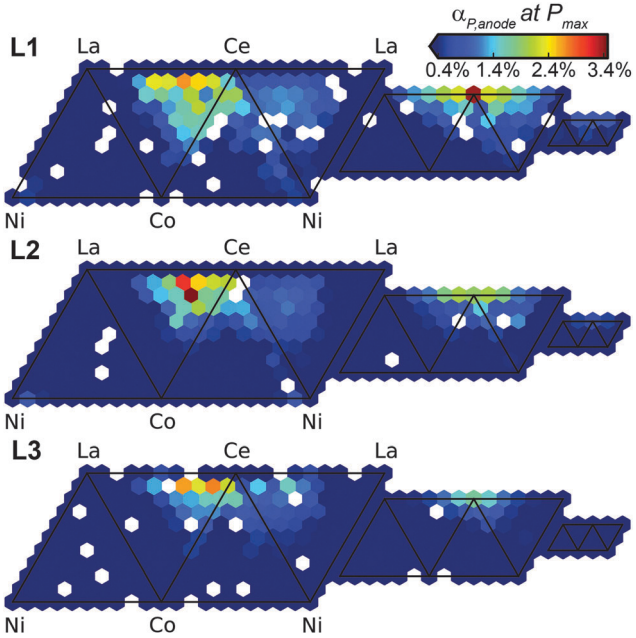

Fig. 10 Power conversion efficiency ($\alpha_{P,anode}$) for each photoanode at its maximum power point. The conversion efficiency is calculated as the ratio of the maximum electrochemical power generation (P_{max}) to the consumed optical power (reflected or absorbed irradiation, $P_{consumed}$). For bare $BiVO_4$, this efficiency is below the colour scale at 0.16%.

Conclusions

By combining a uniform $BiVO_4$ thin film light absorber and a discrete library of (Ni–La–Co–Ce)O_x coatings, we created 858 catalyst/$BiVO_4$ assemblies covering a wide range of metal oxide compositions at three different loadings. Each assembly was evaluated as a solar fuels photoanode in pH 13 using automated photoelectrochemistry with *in situ* optical characterization, providing a robust, high throughput identification of the metal oxide coatings that greatly enhance the OER photoelectrocatalytic activity. The high throughput discovery of new high performance catalyst/$BiVO_4$ photoanodes was verified through traditional characterization of a scaled-up $La_{0.2}Co_{0.2}Ce_{0.6}O_x/BiVO_4$ electrode

that produced a photovoltage of 0.81 V under AM 1.5 illumination, which is in the top tier of thin-film $BiVO_4$ photoanodes at high pH. We anticipate that the findings presented here could also be incorporated into the design of high efficiency systems that utilize state-of-the-art approaches to doping, nanostructuring, and heterostructuring of $BiVO_4$. Additional high throughput characterization of the metal oxide coatings enabled a data-driven identification of metal oxide compositions whose performance in integrated photoanodes greatly exceeded predictions, indicating the formation of an improved interface. These metal oxides contain no less than 3 of the Ni–La–Co–Ce elements, demonstrating the importance of high-order composition spaces in interface optimization. The best metal oxide coatings improve the PEC power conversion efficiency 20-fold compared to bare $BiVO_4$, validating the efficacy of the high throughput methodology in discovering high performance photoanodes for incorporation into efficient water splitting devices.

Glossary

$A_{BVO}(\lambda)$	Fractional absorption spectrum of the $BiVO_4$ thin film
CA	Chronoamperometry
CV	Cyclic voltammetry (or cyclic voltammogram)
$E_{AM1.5}(\lambda)$	Spectral irradiance of global air mass 1.5 (ASTM 6173-03)
$E_{lamp}(\lambda)$	Spectral irradiance of the light source used in the high throughput measurements
E_{OC}	Open circuit potential for a photoanode under illumination
E_{mp}	Potential at the maximum power point
J_{cat}	Oxygen evolution reaction current density of an electrocatalyst at 1.58 V *vs.* RHE (0.35 V *vs.* O_2/H_2O).
J_{mp}	Photocurrent density at the maximum power point of a photoanode
J_{O_2/H_2O}	Photocurrent density of a photoanode measured at the Nernstian potential for the oxygen evolution reaction
J_{max}	Maximum relevant electrocatalytic current density for the $BiVO_4$ thin film; defined for the evaluation and prediction of catalyst performance upon integration into a photoanode
$J_{photo}(V)$	Photocurrent density calculated from the high throughput, toggled-illumination CVs
$N_{lamp}(\lambda)$	Photon flux of the light source used in the high throughput measurements
$P_{consumed}$	Total optical power reflected or absorbed by a photoanode and thus no longer available to an underlying photocathode in a tandem light absorber structure
P_{max}	Maximum electrochemical power generation from $J_{photo}(V)$ of a photoanode, which demarcates the maximum power point
$T(\lambda)$	Fractional optical transmission spectrum of a photoanode or electrocatalyst
$T_{anode}(\lambda)$	Fractional optical transmission spectrum of a photoanode
$T_{cat}(\lambda)$	Fractional optical transmission spectrum of an electrocatalyst sample
$\alpha_{C,cat}$	Combined optical-electrocatalytic efficiency of an electrocatalyst used in the evaluation and prediction of performance upon integration into a photoanode
$\alpha_{T,anode}$	Optical transmission efficiency of a photoanode; calculated as the fraction of the 390–900 nm portion of AM 1.5 irradiance that is transmitted to an unspecified photocathode
$\alpha_{T,cat}$	Optical transmission efficiency of an electrocatalyst measured *in situ* at 1.58 V *vs.* RHE; calculated as the fractional transmission of photons that are expected to be absorbed by the light absorber, which is particular to the specific lamp spectrum and thin film $BiVO_4$ of the present work
$\alpha_{P,anode}$	Power conversion efficiency of a photoanode; calculated as the fraction of the consumed optical power that is converted to electrochemical power at the maximum power point
η_{OER}	Overpotential for the OER; potential applied to a catalyst with respect to the O_2/H_2O Nernstian potential
Γ'	Photoanode performance compared to that predicted from the optical and electrical performance of the isolated catalysts; calculated as the log-ratio of the maximum electrochemical power generation of the photoanode and the combined optical-electrocatalytic efficiency of the catalyst
Γ	Relative photoanode performance compared to that predicted from the isolated catalysts; akin to Γ' but shifted so that the median value for the photoanode library is 0

Acknowledgements

This material is based upon work performed by the Joint Center for Artificial Photosynthesis, a DOE Energy Innovation Hub, supported through the Office of Science of the U.S. Department of Energy (Award No. DE-SC0004993). The authors thank Citrine Informatics (www.citrine.io) for data hosting. The raw potentiostat and spectrometer data for the anodic sweep of the CV for each photoanode are available at links.citrination.com/ni-la-co-ce.

Notes and references

1 M. G. Walter, E. L. Warren, J. R. McKone, S. W. Boettcher, Q. Mi, E. A. Santori and N. S. Lewis, *Chem. Rev.*, 2010, **110**, 6446–6473.

2 C. C. L. McCrory, S. Jung, I. M. Ferrer, S. M. Chatman, J. C. Peters and T. F. Jaramillo, *J. Am. Chem. Soc.*, 2015, **137**, 4347–4357.
3 C. C. L. McCrory, S. Jung, J. C. Peters and T. F. Jaramillo, *J. Am. Chem. Soc.*, 2013, **135**, 16977–16987.
4 S. Hu, N. S. Lewis, J. W. Ager, J. Yang, J. R. McKone and N. C. Strandwitz, *J. Phys. Chem. C*, 2015, **119**, 24201–24228.
5 W. A. Smith, I. D. Sharp, N. C. Strandwitz and J. Bisquert, *Energy Environ. Sci.*, 2015, **8**, 2851–2862.
6 J. A. Haber, Y. Cai, S. Jung, C. Xiang, S. Mitrovic, J. Jin, A. T. Bell and J. M. Gregoire, *Energy Environ. Sci.*, 2014, **7**, 682–688.
7 J. A. Haber, C. Xiang, D. Guevarra, S. Jung, J. Jin and J. M. Gregoire, *ChemElectroChem*, 2014, **1**, 524–528.
8 J. A. Haber, D. Guevarra, S. Jung, J. Jin and J. M. Gregoire, *ChemElectroChem*, 2014, **1**, 1613–1617.
9 J. M. Gregoire, C. Xiang, S. Mitrovic, X. Liu, M. Marcin, E. W. Cornell, J. Fan and J. Jin, *J. Electrochem. Soc.*, 2013, **160**, F337–F342.
10 M. L. Green, I. Takeuchi and J. R. Hattrick-Simpers, *J. Appl. Phys.*, 2013, **113**, 231101.
11 T. H. Muster, A. Trinchi, T. A. Markley, D. Lau, P. Martin, A. Bradbury, A. Bendavid and S. Dligatch, *Electrochim. Acta*, 2011, **56**, 9679–9699.
12 R. A. Potyrailo and W. F. Maier, *Combinatorial and High-Throughput Discovery and Optimization of Catalysts and Materials*, Taylor & Francis, 2006.
13 H. Ye, H. S. Park and A. J. Bard, *J. Phys. Chem. C*, 2011, **115**, 12464–12470.
14 R. Saito, Y. Miseki, W. Nini and K. Sayama, *ACS Comb. Sci.*, 2015, **17**, 592–599.
15 M. Barroso, A. J. Cowan, S. R. Pendlebury, M. Grätzel, D. R. Klug and J. R. Durrant, *J. Am. Chem. Soc.*, 2011, **133**, 14868–14871.
16 M. Barroso, C. A. Mesa, S. R. Pendlebury, A. J. Cowan, T. Hisatomi, K. Sivula, M. Grätzel, D. R. Klug and J. R. Durrant, *Proc. Natl. Acad. Sci. U. S. A.*, 2012, **109**, 15640–15645.
17 D. R. Gamelin, *Nat. Chem.*, 2012, **4**, 965–967.
18 K. Sivula, *J. Phys. Chem. Lett.*, 2013, **4**, 1624–1633.
19 G. M. Carroll, D. K. Zhong and D. R. Gamelin, *Energy Environ. Sci.*, 2015, **8**, 577–584.
20 F. Lin and S. W. Boettcher, *Nat. Mater.*, 2014, **13**, 81–86.
21 F. Lin, B. F. Bachman and S. W. Boettcher, *J. Phys. Chem. Lett.*, 2015, **6**, 2427–2433.
22 J. K. Cooper, S. Gul, F. M. Toma, L. Chen, P.-A. Glans, J. Guo, J. W. Ager, J. Yano and I. D. Sharp, *Chem. Mater.*, 2014, **26**, 5365–5373.
23 J. K. Cooper, S. Gul, F. M. Toma, L. Chen, Y.-S. Liu, J. Guo, J. W. Ager, J. Yano and I. D. Sharp, *J. Phys. Chem. C*, 2015, **119**, 2969–2974.
24 A. J. E. Rettie, H. C. Lee, L. G. Marshall, J.-F. Lin, C. Capan, J. Lindemuth, J. S. McCloy, J. Zhou, A. J. Bard and C. B. Mullins, *J. Am. Chem. Soc.*, 2013, **135**, 11389–11396.
25 Y. Liang, T. Tsubota, L. P. A. Mooij and R. van de Krol, *J. Phys. Chem. C*, 2011, **115**, 17594–17598.
26 J. A. Seabold and K.-S. Choi, *J. Am. Chem. Soc.*, 2012, **134**, 2186–2192.
27 F. F. Abdi, L. Han, A. H. M. Smets, M. Zeman, B. Dam and R. van de Krol, *Nat. Commun.*, 2013, **4**, 2195.
28 F. F. Abdi, N. Firet and R. van de Krol, *ChemCatChem*, 2013, **5**, 490–496.
29 W. Luo, Z. Yang, Z. Li, J. Zhang, J. Liu, Z. Zhao, Z. Wang, S. Yan, T. Yu and Z. Zou, *Energy Environ. Sci.*, 2011, **4**, 4046–4051.
30 S. K. Pilli, T. E. Furtak, L. D. Brown, T. G. Deutsch, J. A. Turner and A. M. Herring, *Energy Environ. Sci.*, 2011, **4**, 5028–5034.
31 H. W. Jeong, T. H. Jeon, J. S. Jang, W. Choi and H. Park, *J. Phys. Chem. C*, 2013, **117**, 9104–9112.
32 Y. Park, D. Kang and K.-S. Choi, *Phys. Chem. Chem. Phys.*, 2014, **16**, 1238–1246.
33 K. Zhang, X.-J. Shi, J. K. Kim and J. H. Park, *Phys. Chem. Chem. Phys.*, 2012, **14**, 11119–11124.
34 W. Yao, H. Iwai and J. Ye, *Dalton Trans.*, 2008, 1426–1430, DOI: 10.1039/B713338C.
35 C. Jiang, R. Wang and B. A. Parkinson, *ACS Comb. Sci.*, 2013, **15**, 639–645.
36 X. Shi, I. Y. Choi, K. Zhang, J. Kwon, D. Y. Kim, J. K. Lee, S. H. Oh, J. K. Kim and J. H. Park, *Nat. Commun.*, 2014, **5**, 4775.
37 P. M. Rao, L. Cai, C. Liu, I. S. Cho, C. H. Lee, J. M. Weisse, P. Yang and X. Zheng, *Nano Lett.*, 2014, **14**, 1099–1105.
38 S. J. Hong, S. Lee, J. S. Jang and J. S. Lee, *Energy Environ. Sci.*, 2011, **4**, 1781–1787.
39 Y. Pihosh, I. Turkevych, K. Mawatari, J. Uemura, Y. Kazoe, S. Kosar, K. Makita, T. Sugaya, T. Matsui, D. Fujita, M. Tosa, M. Kondo and T. Kitamori, *Sci. Rep.*, 2015, **5**, 11141.
40 J. Su, L. Guo, N. Bao and C. A. Grimes, *Nano Lett.*, 2011, **11**, 1928–1933.
41 T. W. Kim and K.-S. Choi, *Science*, 2014, **343**, 990–994.
42 A. Loiudice, J. K. Cooper, L. H. Hess, T. M. Mattox, I. D. Sharp and R. Buonsanti, *Nano Lett.*, 2015, **15**, 7347–7354.
43 C. Ding, J. Shi, D. Wang, Z. Wang, N. Wang, G. Liu, F. Xiong and C. Li, *Phys. Chem. Chem. Phys.*, 2013, **15**, 4589–4595.
44 M. T. McDowell, M. F. Lichterman, J. M. Spurgeon, S. Hu, I. D. Sharp, B. S. Brunschwig and N. S. Lewis, *J. Phys. Chem. C*, 2014, **118**, 19618–19624.
45 D. E. Wang, R. G. Li, J. Zhu, J. Y. Shi, J. F. Han, X. Zong and C. Li, *J. Phys. Chem. C*, 2012, **116**, 5082–5089.
46 F. F. Abdi and R. van de Krol, *J. Phys. Chem. C*, 2012, **116**, 9398–9404.
47 D. Wang, R. Li, J. Zhu, J. Shi, J. Han, X. Zong and C. Li, *J. Phys. Chem. C*, 2012, **116**, 5082–5089.
48 D. K. Zhong, S. Choi and D. R. Gamelin, *J. Am. Chem. Soc.*, 2011, **133**, 18370–18377.
49 T. H. Jeon, W. Choi and H. Park, *Phys. Chem. Chem. Phys.*, 2011, **13**, 21392–21401.
50 M. Zhou, J. Bao, W. Bi, Y. Zeng, R. Zhu, M. Tao and Y. Xie, *ChemSusChem*, 2012, **5**, 1420–1425.
51 Q. Jia, K. Iwashina and A. Kudo, *Proc. Natl. Acad. Sci. U. S. A.*, 2012, **109**, 11564–11569.

52 L. Chen, F. M. Toma, J. K. Cooper, A. Lyon, Y. Lin, I. D. Sharp and J. W. Ager, *ChemSusChem*, 2015, **8**, 1066–1071.
53 J. A. Seabold, K. Zhu and N. R. Neale, *Phys. Chem. Chem. Phys.*, 2014, **16**, 1121–1131.
54 J. Gan, X. Lu, B. B. Rajeeva, R. Menz, Y. Tong and Y. Zheng, *ChemElectroChem*, 2015, **2**, 1385–1395.
55 S. K. Choi, W. Choi and H. Park, *Phys. Chem. Chem. Phys.*, 2013, **15**, 6499–6507.
56 K. Walczak, Y. Chen, C. Karp, J. W. Beeman, M. Shaner, J. Spurgeon, I. D. Sharp, X. Amashukeli, W. West, J. Jin, N. S. Lewis and C. Xiang, *ChemSusChem*, 2015, **8**, 544–551.
57 M. R. Singh, K. Papadantonakis, C. Xiang and N. S. Lewis, *Energy Environ. Sci.*, 2015, **8**, 2760–2767.
58 M. F. Lichterman, M. R. Shaner, S. G. Handler, B. S. Brunschwig, H. B. Gray, N. S. Lewis and J. M. Spurgeon, *J. Phys. Chem. Lett.*, 2013, **4**, 4188–4191.
59 J. A. Haber, E. Anzenburg, J. Yano, C. Kisielowski and J. M. Gregoire, *Adv. Energy Mater.*, 2015, **5**, 11.
60 A. Shinde, D. Guevarra, J. A. Haber, J. Jin and J. M. Gregoire, *J. Mater. Res.*, 2015, **30**, 442–450.
61 D. A. Corrigan, *J. Electrochem. Soc.*, 1987, **134**, 377–384.
62 L. Trotochaud, S. L. Young, J. K. Ranney and S. W. Boettcher, *J. Am. Chem. Soc.*, 2014, **136**, 6744–6753.
63 S. Klaus, Y. Cai, M. W. Louie, L. Trotochaud and A. T. Bell, *J. Phys. Chem. C*, 2015, **119**, 7243–7254.
64 S. Mitrovic, E. W. Cornell, M. R. Marcin, R. J. R. Jones, P. F. Newhouse, S. K. Suram, J. Jin and J. M. Gregoire, *Rev. Sci. Instrum.*, 2015, **86**, 013904.
65 R. H. Coridan, A. C. Nielander, S. A. Francis, M. T. McDowell, V. Dix, S. M. Chatman and N. S. Lewis, *Energy Environ. Sci.*, 2015, **8**, 2886–2901.
66 L. Trotochaud, T. J. Mills and S. W. Boettcher, *J. Phys. Chem. Lett.*, 2013, **4**, 931–935.

